



# The Infrared Evolution of Dust in V838 Monocerotis

C. E. Woodward<sup>1</sup> , A. Evans<sup>2</sup> , D. P. K. Banerjee<sup>3</sup> , T. Liimets<sup>4,5</sup> , A. A. Djupvik<sup>6</sup> , S. Starrfield<sup>7</sup> , G. C. Clayton<sup>8</sup> ,  
S. P. S. Eyres<sup>9</sup> , R. D. Gehrz<sup>1</sup> , and R. M. Wagner<sup>10,11</sup>

<sup>1</sup> Minnesota Institute for Astrophysics, University of Minnesota, 116 Church Street SE, Minneapolis, MN 55455, USA; [chickw024@gmail.com](mailto:chickw024@gmail.com)

<sup>2</sup> Astrophysics Group, Keele University, Keele, Staffordshire, ST5 5BG, UK

<sup>3</sup> Physical Research Laboratory, Navrangpura, Ahmedabad, Gujarat 380009, India

<sup>4</sup> Astronomický ústav, Akademie věd České republiky, v.v.i., Fričova 298, 251 65 Ondřejov, Czech Republic

<sup>5</sup> Tartu Observatory, University of Tartu, Observatooriumi 1, 61602 Tõravere, Estonia

<sup>6</sup> Nordic Optical Telescope, Rambla José Ana Fernández Pérez 7, ES-38711 Breña Baja, Spain

<sup>7</sup> School of Earth and Space Exploration, Arizona State University, Box 871404, Tempe, AZ 85287-1404, USA

<sup>8</sup> Louisiana State University, Baton Rouge, Department of Physics & Astronomy Baton Rouge, LA 70803-001, USA

<sup>9</sup> Faculty of Computing, Engineering & Science, University of South Wales, Pontypridd, CF37 1DL, UK

<sup>10</sup> Department of Astronomy, The Ohio State University, 140 W. 18th Avenue, Columbus, OH 43210, USA

<sup>11</sup> Large Binocular Telescope Observatory, 933 North Cherry Avenue, Tucson, AZ 85721, USA

Received 2021 June 20; revised 2021 August 16; accepted 2021 August 17; published 2021 October 7

## Abstract

Luminous Red Variables are most likely eruptions that are the outcome of stellar mergers. V838 Mon is one of the best-studied members of this class, representing an archetype for stellar mergers resulting from B-type stars. As result of the merger event, “nova-like” eruptions occur driving mass loss from the system. As the gas cools considerable circumstellar dust is formed. V838 Mon erupted in 2002 and is undergoing very dynamic changes in its dust composition, geometry, and infrared luminosity providing a real-time laboratory to validate mineralogical condensation sequences in stellar mergers and evolutionary scenarios. We discuss recent NASA Stratospheric Observatory for Infrared Astronomy 5–38  $\mu\text{m}$  observations combined with archival NASA Spitzer spectra that document the temporal evolution of the freshly formed (within the last  $\lesssim 20$  yr) circumstellar material in the environs of V838 Mon. Changes in the 10  $\mu\text{m}$  spectral region are strong evidence that we are witnessing a classical dust condensation sequence expected to occur in oxygen-rich environments where alumina formation is followed by that of silicates at the temperature cools.

*Unified Astronomy Thesaurus concepts:* Asymptotic giant branch stars (2100); Circumstellar dust (236); Astrochemistry (75)

*Supporting material:* data behind figure

## 1. Introduction

Luminous Red Variables (LRVs) are characterized by very high luminosities, low effective temperatures, long ( $\gtrsim 200$  day) evolution timescales of the eruption, and consequently large eruption energies (see Figure 1 in Kasliwal 2012). They also display the presence of gas-phase AlO, SiO, SO, SO<sub>2</sub> and occasionally H<sub>2</sub>S emission and/or absorption (Kamiński et al. 2018), dusty circumstellar disks that show evidence of alumina (Al<sub>2</sub>O<sub>3</sub>), and other solid oxides (Banerjee et al. 2015). Their high luminosity at maximum (Bond & Siegel 2006;  $M_{\text{bol}} \sim -10$  with  $M_v \lesssim -9$ , surpassing typical classical novae at maximum,  $M_v \lesssim -8$ ) is confirmed by the detection of LRVs in M31 (Bond & Siegel 2006) and in other galaxies (Kasliwal 2012; Williams et al. 2015; Smith et al. 2016). While their nature was initially unclear (with nova eruptions, planet-swallowing stars, and very late thermal pulses having been suggested) the “best-bet” scenario, based on V1309 Sco, is the merger of two stars (Tyndea & Soker 2006; MacLeod & Loeb 2020; Pastorello et al. 2021) within a triple or higher system (Kamiński et al. 2021). Pastorello et al. (2019) present a recent extensive review of the phenomena.

V838 Mon is the best-studied LRV. Shortly after its eruption in 2002 (Brown et al. 2002), a light echo—due to reflection of the eruption off circumstellar dust—became very prominent (Bond et al. 2003). The echo was also prominent in Spitzer (+MIPS; Banerjee et al. 2006) and Herschel (Exter et al. 2016) imagery at  $\lambda \gtrsim 70 \mu\text{m}$ . V838 Mon is 6.2 kpc distant, a value tightly constrained from polarized light echo studies (Sparks et al. 2008).

Early in the eruption it displayed AlO, TiO, and VO bands in the near-infrared (Banerjee & Ashok 2002; Evans et al. 2003; Lynch et al. 2004). Evans et al. (2003) classified V838 Mon as an “L supergiant,” with an effective temperature  $T_{\text{eff}} \lesssim 2300$  K. Over the period 2002 through 2004 there were several absorption features present that are due to rotational-vibrational transitions in water (Banerjee et al. 2005). Banerjee et al. (2005) concluded that the water arises from a cool  $\sim 800$  K region, and that the excitation temperature and water column density were decreasing with time; this latter temperature was consistent with that deduced by Lynch et al. (2004). As of 2009, however, Loebman et al. (2015) concluded that the ejected material was at a radial distance of  $\simeq 263$  au and had temperature of 285 K. Chesneau et al. (2014) found that V838 Mon is surrounded by a flattened dusty structure (position angle  $-10^\circ$ ) that is likely transitory and extends to several hundred au from the central star based on mid-infrared interferometric imagery. Exter et al. (2016) found an extended source region of cold dust



Original content from this work may be used under the terms of the [Creative Commons Attribution 4.0 licence](https://creativecommons.org/licenses/by/4.0/). Any further distribution of this work must maintain attribution to the author(s) and the title of the work, journal citation and DOI.

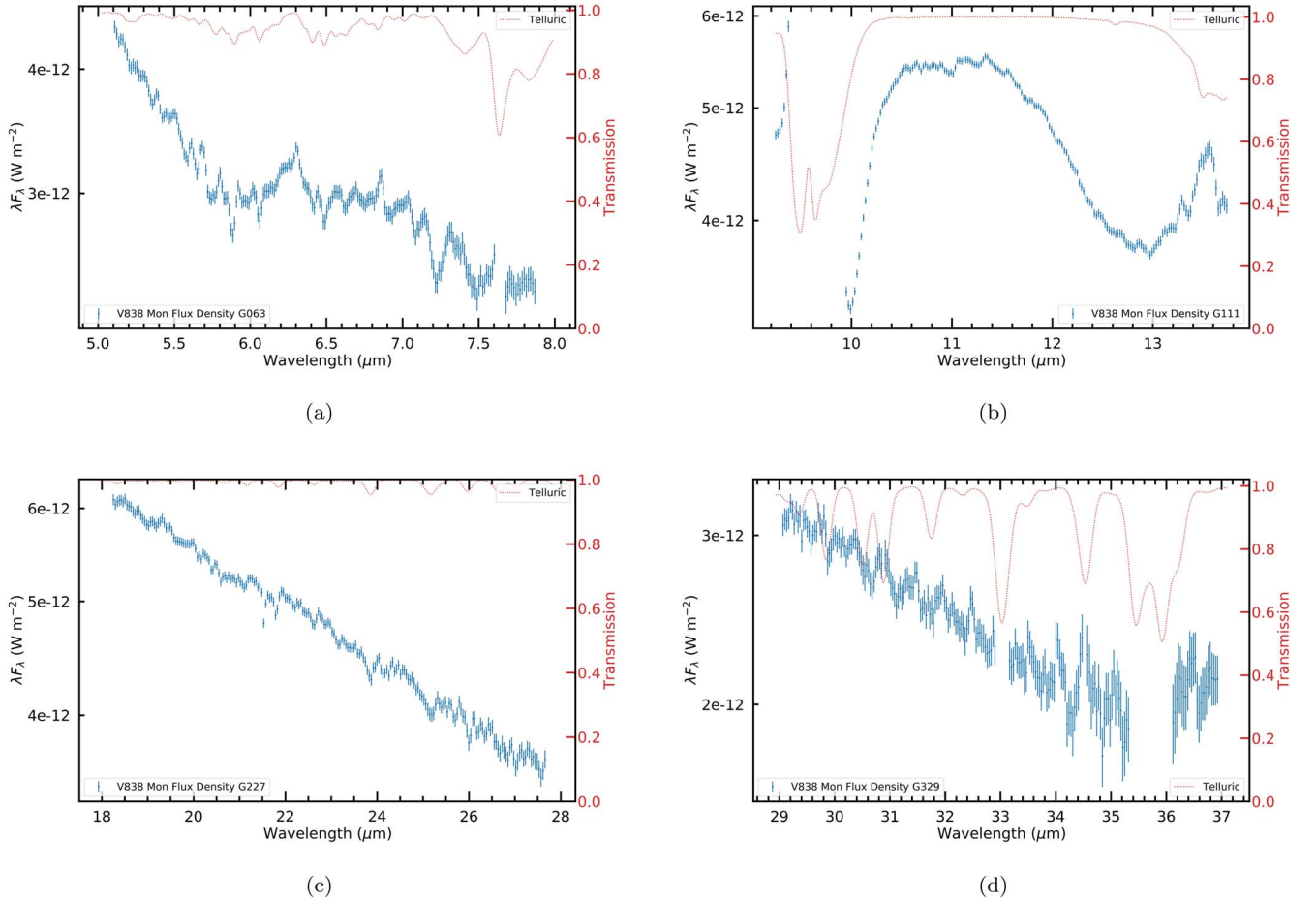


**Figure 1.** V838 Mon SOFIA FORCAST spectra shown by individual grating to highlight spectral details and the signal-to-noise quality of the data. The panels are (a) G063, (b) G111, (c) G227, and (d) G329. The G063 and the G111 spectra are averages of two different observations on separate and distinct flight missions (the difference in the spectral calibration were within the CALERR uncertainties; Table 1). The uncertainties at a given spectral data point were propagated in quadrature. The dotted red line depicts the model atmospheric transmission at the flight altitude of the observations. Gaps in the contiguous spectral coverage arise from regions where the atmospheric transmission was modeled to be  $\lesssim 70\%$ .

(The data used to create this figure are available.)

emission  $\approx 2.7$  pc in size ( $\sim 1/5$  in diameter) surrounding V838 Mon. Similar structures are seen other post-AGB giant oxygen-rich systems, such as 89 Her (Hillen et al. 2014), using interferometric techniques.

Here we present recent observations of V838 Mon obtained with the NASA Stratospheric Observatory for Infrared Astronomy (SOFIA; Gehrz et al. 2009; Young et al. 2012). The objective was to investigate the nature and dynamic evolution of the system’s dust that formed in the material ejected by the stellar merger.

We find significant changes in dust chemistry in the circumstellar environment. Comparison of the recent SOFIA measurement of the spectral energy distribution to prior Spitzer spectra obtained almost a decade earlier suggests that in the  $10\ \mu\text{m}$  region we are observing signatures of a “classical” dust condensation sequence that is expected to occur in oxygen-rich environments (Tielens 1990; Karovicova et al. 2013) where alumina ( $\text{Al}_2\text{O}_3$ ) forms initially in the hot,  $T \sim 1700$  K dust envelope (Speck et al. 2000) followed by the formation of various silicates at cooler temperatures of  $T \simeq 1200$  K (Tielens et al. 1998; Gail & Hoppe 2010).

## 2. Observations and Data Reduction

Mid-infrared observations of V838 Mon were conducted in 2019 October on three consecutive flight originating from Palmdale, CA, with the SOFIA airborne observatory using the Faint Object InfraRed Camera (FORCAST; Herter et al. 2018), the dual-channel mid-infrared imager and grism spectrometer operating from  $5\text{--}40\ \mu\text{m}$ , mounted at the Nasmyth focus of the 2.5 m telescope. V838 Mon was imaged (platescale of  $0''.768$  per pixel) in the mid-infrared in three filters: F7.7 ( $\Delta\lambda = 0.47\ \mu\text{m}$ ) narrow band, F11.2 ( $\Delta\lambda = 2.7\ \mu\text{m}$ ), and F31.5 ( $\Delta\lambda = 5.7\ \mu\text{m}$ ); as well as the Short Wavelength Camera (SWC) grism (G063) on the first flight, while on the second flight imaging in the F197.7 ( $\Delta\lambda = 5.5\ \mu\text{m}$ ) and F37.1 ( $\Delta\lambda = 3.3\ \mu\text{m}$ ) filters was performed in addition to Long Wavelength Camera (LWC) grism observations with three gratings (G111, G227, and G329). On the third night the grism G063 and G111 observations were repeated.

For all spectroscopic observations the instrument was configured using a long slit ( $4''.7 \times 191''$ ), which yields a spectral resolution  $R = \lambda/\Delta\lambda \sim 140\text{--}300$ . The position angle

**Table 1**  
FORCAST Observational Summary-V838 Mon<sup>a</sup>

Mean Observation 2019 UT Date (mm-dd hr:min:s)	Instrument Configuration	Grism or Filter $\lambda_{\text{eff}}$ ( $\mu\text{m}$ )	Single Frame Exposure Time (s)	Total On Source Integration Time (s)	CALERR <sup>b</sup>
(FO F628)					
s 10-23T09:36:29.9	Imaging Dual	7.7	25.66	359.20	...
10-23T09:58:02.8	Imaging Dual	11.2	27.07	324.88	...
10-23T09:36:29.9	Imaging Dual	31.5	26.34	640.18	...
10-23T08:50:20.2	Grism SWC	G063	19.92	637.47	0.0348
(FO_F629)					
10-24T10:33:13.7	Imaging Dual	19.7	26.15	313.78	...
10-24T10:33:13.7	Imaging Dual	37.1	26.15	313.78	...
10-24T08:07:41.8	Grism LWC	G111	34.37	1031.17	0.0743
10-24T08:52:02.0	Grism LWC	G227	34.31	1029.40	0.0055
10-24T09:36:18.3	Grism LWC	G329	32.28	2388.36	0.0136
(FO_F630)					
10-25T09:40:11.9	Grism SWC	G063	13.34	213.39	0.0348
10-25T10:02:45.7	Grism LWC	G111	32.57	586.20	0.0743

**Notes.**

<sup>a</sup> Data files are available through the Infrared Processing and Analysis Center Infrared Science Archives at <https://dcs.arc.nasa.gov>.

<sup>b</sup> Pipeline systematic photometric calibration error for the grating.

of the slit was arbitrary. V838 Mon was imaged with short 9 sec exposures in the SWC using the F111 filter to position the target in the slit. Both imaging and spectroscopic data were obtained using a two-point chop/nod in the Nod-Match-Chop (C2N) mode with 45'' chop and 90'' nod amplitudes at angles of 30°/210° in the equatorial reference frame. Flight altitudes were  $\approx 13,100$  m.

Table 1 summarizes the all observational data sets discussed herein.

### 2.1. *SOFIA Spectra*

The FORCAST scientific data products were retrieved from the Infrared Processing and Analysis Center (IPAC) Infrared Science Archives (IRSA) after standard pipeline processing and flux calibration was performed (for details see Clarke et al. 2015). Computed atmospheric transmission models for the flight altitudes (which are contained in the data products) were used to mask out grism data points in wavelength regions where the transmission was less than 70%. Spectra with grisms G063 and the G111 were obtained on two separate and distinct flight missions. However, the spectral energy distributions (SEDs) did not vary in shape or average intensity between the flights (i.e., the source was not detected to be varying on a timescale of  $\lesssim 72$  hr) and the difference in the spectral calibration were within the pipeline CALERR (systematic) uncertainties. Hence these data were averaged into a single spectrum for each grating. Figure 1 presents panels for each individual grating segment, spanning their respective spectral free range, to illustrate details of the observed SED.

### 2.2. *SOFIA Imagery*

Images of V838 Mon were obtained on two different nights (see Table 1). Azimuthally averaged radial profiles of V838 Mon in each filter exhibited some evidence of extended emission beyond the point-spread function (PSF) of point sources observed with FORCAST under optimal telescope

jitter performance in each filter.<sup>12</sup> The mean full width half maximum (FWHM) of the azimuthally averaged radial profiles of the V838 Mon image data was  $3''.00 \pm 0''.27$  (i.e.,  $3.91 \pm 0.35$  pixels). Centroiding on the photocenter of V838 Mon, photometry in an effective circular aperture of diameter of  $10''.75$  (i.e., a photometric aperture equivalent to  $\approx 3 \times$  the observed source FWHM), with a background aperture annulus of inner radius 12 pixels ( $9''.22$ ) and outer radius of 17 pixels ( $13''.01$ ) was performed on the Level 3 pipeline coadded (\*, COA) image data products using the Aperture Photometry Tool (APT v2.4.7; Laher et al. 2012). Sky-annulus median subtraction (ATP Model B as described in Laher et al. 2012) was used in the computation of the source intensity. The random source intensity uncertainty was computed using a depth of coverage value equivalent to the number of coadded image frames. The calibration factors (and associated uncertainties) applied to the resultant aperture sums were included in the Level 3 data distribution and were derived from the weighted average calibration observations of  $\alpha$  Ceti or  $\alpha$  Tau. The resultant SOFIA photometry is presented in Table 2.

Figure 2 provides  $30''.72 \times 30''.72$  postage-stamp gray-scale images with superimposed surface brightness contours. Generally the images are point like, although the 7.7 through  $19.7 \mu\text{m}$  images are slightly elongated at low surface brightness, with a position angle (PA; East of North) of  $\sim 56^\circ$ . This elongation may be associated with bipolar lobes of dust emission, perpendicular to the flattened-disk (derived major axis size 23 mas at  $8 \mu\text{m}$  and 70 mas at  $13 \mu\text{m}$ ) structure interferometrically detected from 8–13  $\mu\text{m}$  by Chesneau et al. (2014), which has a major axis PA of  $-10^\circ$ . Given the FORCAST platescale and the beam FWHM (which has telescope jitter effects), SOFIA would not be able to directly detect such a structure even at  $\lambda \geq 30 \mu\text{m}$ . However, the SOFIA elongation in the low-surface-brightness emission is similar in the position angle to that of the SiO maser emission

<sup>12</sup> <http://www.sofia.usra.edu/Science/ObserversHandbook/FORCAST.html>

**Table 2**  
V838 Mon Photometry<sup>a</sup>

Filter ( $\mu\text{m}$ )	Flux Density (Jy)	Flux ( $\times 10^{-12} \text{ W m}^{-2}$ )
7.7	$5.912 \pm 0.059$	$2.302 \pm 0.023$
11.2	$19.416 \pm 0.074$	$5.197 \pm 0.020$
19.7	$38.454 \pm 0.088$	$5.852 \pm 0.013$
31.5	$26.161 \pm 0.077$	$2.490 \pm 0.007$
37.1	$17.527 \pm 0.266$	$1.416 \pm 0.021$

**Note.**

<sup>a</sup> Measured in a circular aperture with a diameter of  $10''.75$  centroided on the photocenter of V838 Mon in each SOFIA FORCAST image at a given filter.

channel velocity maps observed after 2018 November 20 (Ortiz-León et al. 2020). The  $11.2 \mu\text{m}$  SOFIA image also has a secondary source (likely a background source)  $12''.60$  to the southwest of V838 Mon with a flux density (in a  $10''.75$  diameter aperture) of  $1.23 \pm 0.07 \text{ Jy}$ .

### 2.3. Spitzer Spectra

To study the long-term spectral evolution of the circumstellar material, reduced archival Spitzer Infrared Spectrograph (IRS; Houck et al. 2004) high-resolution spectra (optimal difference extraction of nod1 and nod2) of V838 Mon also were retrieved from the Combined Atlas of Sources with Spitzer IRS Spectra<sup>13</sup> (Lebouteiller et al. 2015, 2011) from high-spectral resolution observations conducted on 2005 March 17.6139 (AORKey 10523136) and 2008 December 10.0133 (AORKey 2543355).

### 2.4. Ancillary Optical and Near-infrared Photometry

Subsequent to outburst and initial decline of the light curve toward quiescence, optical BVIR photometry of V838 Mon acquired since JD 245 7648.91 (2016 Sept 17) through JD 245 933.53 (2021 April 26) in the AAVSO<sup>14</sup> database (Kafka 2020) show that there has been little ( $\lesssim 0.5 \text{ mag}$ ) change in the light curve; it has remained essentially flat at all bands.

V838 Mon was observed with The Nordic Optical Telescope’s near-infrared camera and spectrograph (NOTCam), using its high-resolution camera ( $0''.079$  per pixel<sup>-1</sup>; Abbott et al. 2000) the broadband filters  $J$ ,  $H$ , and  $K_s$  filters on 2020 March 02, JD 245 8911.43715 (the midpoint of the observations), a few months after the 2019 SOFIA flights. Photometric calibration was performed using three 2MASS stars in the field of view of the images and standard fields at a similar airmass observed just before the target. Standard infrared imaging reduction techniques using IRAF<sup>15</sup> and apertures photometry ( $7''.0$  circular diameter). The error (in magnitudes) is dominated by the uncertainty in the calibration stars.

The observed near-infrared photometry,  $J = 6.59 \pm 0.05$ ,  $H = 5.55 \pm 0.05$ ,  $K_s = 4.76 \pm 0.05$ , and AAVSO photometry from JD 245 8879.565 of  $B = 15.65 \pm 0.07$ ,  $V = 13.31 \pm 0.04$ ,

$R = 11.47 \pm 0.03$ , and  $I = 9.47 \pm 0.01$  were dereddened adopting an  $E(B - V) = 0.87$  (see Loebman et al. 2015) with a standard galactic extinction curve (Rieke & Lebofsky 1985). The dereddened photometric data are used later in the analysis to constrain the SED at short wavelengths.

## 3. Discussion

The process of mass loss and dust condensation is unknown for mergers, and the synoptic study (temporal periods of several 100 s of days to 10 s of years) of V838 Mon may provide the constraints to confront observations with theoretical predictions. The nature and *dynamic evolution* of the dust that forms in the material ejected by a stellar merger is not well understood. Observations of V4332 Sgr (another proposed stellar merger) suggest that the grains have a alumina component (Banerjee et al. 2007, 2015), which would be consistent with the strong AIO features in oxygen-rich environments.

### 3.1. The SOFIA 2019 Spectra

The SOFIA spectra (Figure 1) exhibit interesting details regarding the SED of V838 Mon. At wavelengths longwards of  $18 \mu\text{m}$  the spectra are devoid of any strong line emission from hydrogen, helium, or forbidden lines such as [O IV]  $25.91 \mu\text{m}$ , which is a strong coolant present in the late evolution of novae when electron densities in the ejecta are less than  $\sim 10^6 - 10^7 \text{ cm}^{-3}$  (Evans & Gehrz 2012; Helton et al. 2012; Gehrz et al. 2015). No molecular absorption bands or broad features from dust are evident. For example broad amorphous silicate dust emission near  $18 \mu\text{m}$  or (Mg, Fe)O features near  $19.5 \mu\text{m}$  (Posch et al. 2002) are not present.

The 8–14  $\mu\text{m}$  segment of the SED of V838 Mon is complex, being dominated by dust features, including a deep silicate absorption band centered near  $10 \mu\text{m}$ , an amorphous alumina ( $\text{Al}_2\text{O}_3$ ) emission feature near  $\sim 11.3 \mu\text{m}$ , and a  $13 \mu\text{m}$  feature that may be evidence of high temperature spinel ( $\text{MgAl}_2\text{O}_4$ ; Posch et al. 1999; Zeidler et al. 2013). However, the measured FWHM of this latter feature ( $\lambda_o = 13.53 \mu\text{m}$ ) is of an order of  $\sim 0.1 \mu\text{m}$ , which is much narrower than the bandwidth measurements of high temperature ( $300 \lesssim T(K) \lesssim 928$ ) spinels (Table 8 in Zeidler et al. 2013). In addition, expected weaker  $32 \mu\text{m}$  spinel emission bands are not evident in the SOFIA data. Measurement of the  $10 \mu\text{m}$  feature depth,  $\tau_{9.7}$  is challenged by regions of poor atmospheric transmission in the SOFIA SED. A more detailed discussion and modeling of the SED is discussed below (Section 3.3).

From 5.0–8.0  $\mu\text{m}$  (Figure 1(a)), the SED is a composite of emission from the Rayleigh–Jeans tail of the stellar 2300 K blackbody and emission from a cooler dust component. Superposed on the continuum there are a few suggestive emission features. Figure 3 shows the continuum subtracted residual emission, highlighting potential emission features. Features near  $6.30 \mu\text{m}$  and  $6.85 \mu\text{m}$  have been associated with water vapor emission ( $\nu_2$  bands) and formaldehyde ( $\text{H}_2\text{CO}$ ) in spectra of the dense circumstellar disk environments of T Tauri stars (Sargent et al. 2014). Higher spectral resolution observations with instruments like EXES (Richter et al. 2018) on SOFIA or MIRI on the James Webb Space Telescope (JWST) are necessary to confirm these identifications.

<sup>13</sup> <https://cassis.sirtf.com/atlas/>

<sup>14</sup> Observations from the AAVSO International Database, <https://www.aavso.org/database>.

<sup>15</sup> IRAF is distributed by the National Optical Astronomy Observatories, which are operated by the Association of Universities for Research in Astronomy, Inc., under cooperative agreement with the National Science Foundation.



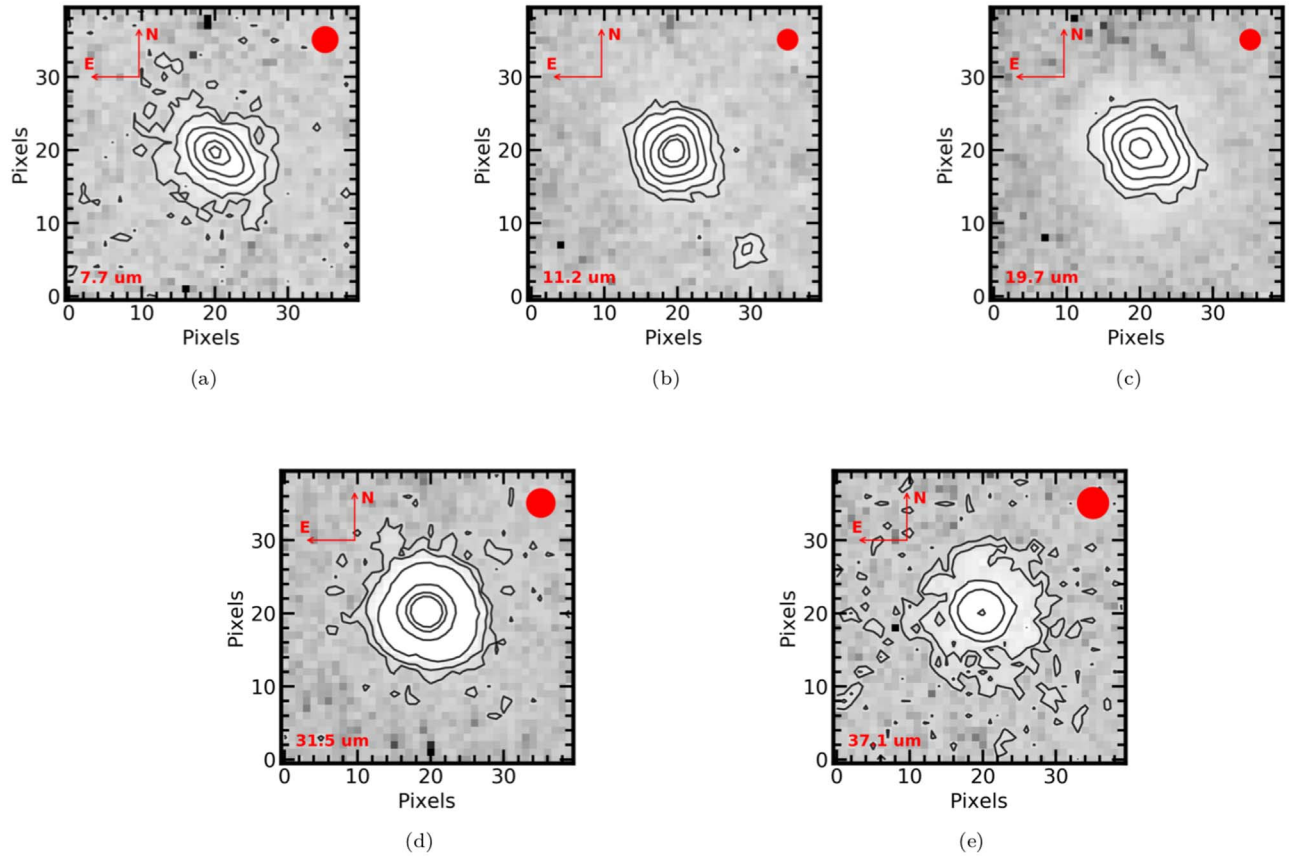


**Figure 2.** SOFIA FORCAST gray-scale images of a  $30''.72 \times 30''.72$  (camera platescale  $0''.768$  per pixel) field of view centered on V838 Mon with superposed isophotal surface brightness contours, where the outermost contour is  $4\sigma$  above the median sky background (Jy per pixel) measured off source. With FORCAST, diffraction limited imaging is possible for  $\lambda \geq 15 \mu\text{m}$ , limited by telescope tracking and jitter. The FWHM PSF for each filter is given by the filled red circle in the upper right corner of each panel. (a) Filter F7.7, with contours at 0.0028 ( $4\sigma$ ), 0.0062, 0.0173, 0.0518, 0.1725, and 0.2829 Jy. (b) Filter F112, with contours at 0.0060 ( $4\sigma$ ), 0.0135, 0.0375, 0.1125, 0.3750, and 0.6160 Jy. (c) Filter F197, with contours at 0.0200 ( $4\sigma$ ), 0.0450, 0.1250, 0.3750, and 1.2500 Jy. (d) Filter F315 with contours at 0.0055 ( $4\sigma$ ), 0.0124, 0.0345, 0.1034, 0.3450, and 0.5658 Jy. (e) Filter F371 with contours at 0.0112 ( $4\sigma$ ), 0.0252, 0.0700, 0.2100, and 0.7000 Jy.

### 3.2. SED Evolution and Dust Emission

Spitzer spectra between 2005 and 2008 show that the mid-IR SEDs is evolving as shown in Figure 4(a). In 2005 the SED is smooth with little evidence for any broad dust emission features; a blackbody fit to the SED yields a dust temperature of  $T_{\text{bb}} = 425 \pm 1.2$  K. No  $10 \mu\text{m}$  feature is evident although it is difficult to draw a definite conclusion because the spectrum is saturated below  $10 \mu\text{m}$ . Three years later, the SED has markedly evolved, broad emission features are present, and at long wavelengths ( $\lambda \geq 20 \mu\text{m}$ ) the SED has a contribution from a cooler dust component.

The 2019 SOFIA SED is similar to that observed by Spitzer in 2008 only at wavelengths  $\geq 18.0 \mu\text{m}$  as shown in Figure 4(b). The flux density in the 9 to  $14 \mu\text{m}$  region, Figure 4(b) observed in 2019 by SOFIA has decreased by  $\sim 38\%$  and exhibits a distinct broad ( $\Delta\lambda \simeq 2.2 \mu\text{m}$ ) emission band, a very distinct  $10 \mu\text{m}$  absorption feature as illustrated in Figure 4(c).

### 3.3. DUSTY Models

To characterize the observed changes due to dust formation and evolution in V838 Mon, we modeled the system using the radiative transfer code DUSTY-DISK, which is similar to the original DUSTY code (Ivezic & Elitzur 1995), but incorporates an additional disk component, appropriate for the case of V838 Mon.

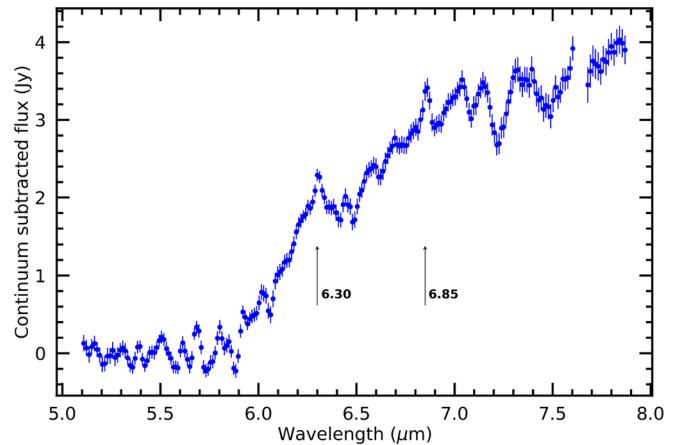


**Figure 3.** Continuum subtracted SOFIAFORCAST spectra of V838 Mon from 5.0–8.0  $\mu\text{m}$ . A second-order Chebyshev polynomial fit using wavelengths from 5.2–5.6  $\mu\text{m}$ , which are on the Rayleigh–Jeans tail of the stellar 2300 K blackbody, was used to determine the local continuum. Features are indicated by the arrows.

For the modeling two grain compositions were considered: silicate grains with optical properties described by Draine & Lee (1984); and amorphous, porous alumina (Begemann et al. 1997). These are bare grains, with no ice coatings. Typical spectral indicators for ice-mantled grains are not seen in V838 Mon. The water ice feature at  $3.05 \mu\text{m}$  (due to and O–H

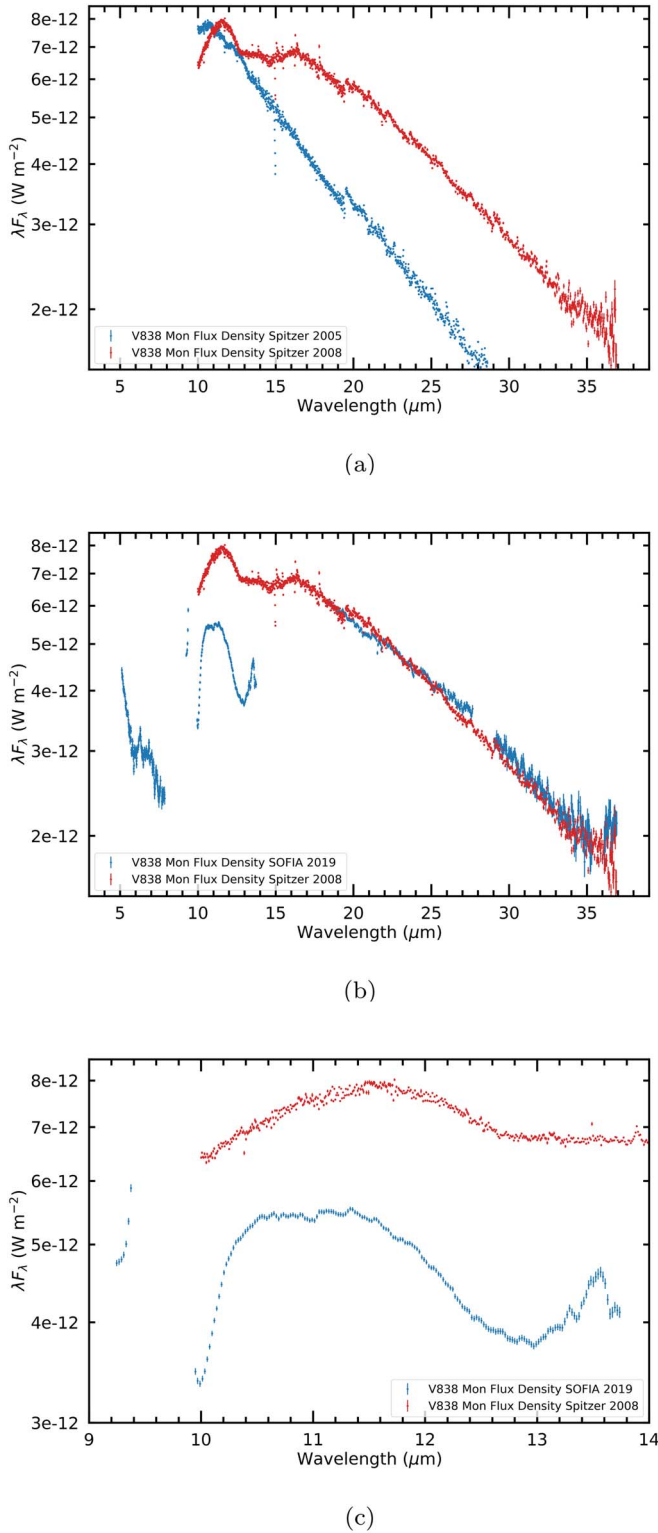


**Figure 4.** Evolution of the infrared spectral energy distribution of V838 Mon. (a) The 2005 Spitzer IRS spectra (blue symbols) and the Spitzer 2008 IRS spectra (red symbols) show the slowly evolving spectral energy distribution, including the emergence of silicate emission bands, especially in the 10 μm region between the two epochs. (b) Comparison of the composite 2019 SOFIA 5–36 μm FORCAST spectra (blue symbols) and the 2008 Spitzer 10–40 μm IRS spectra (red symbols). Gaps in the SOFIA SED are due to noncontiguous spectral coverage of the FORCAST grisms. (c) Same as (b) but highlighting the the region between 9 and 14 μm in detail, which shows the marked change of structure in the 10 μm feature.

stretch mode) is not seen (see Figure 2 in Lynch et al. 2004) nor is the 6.02 μm H–O–H bending mode detected in archival Spitzer low-resolution IRS spectra (which are unsaturated at  $\lambda \lesssim 8$  μm) shortly after outburst. Inspection of the SOFIA spectra near 6.02 μm (Figure 3) also shows no signature of a broad ice absorption feature.

Grids of simple models that varied the relative ratios of these two grain components were constructed, adopting a Mathis–Rumpl–Nordsieck (Mathis et al. 1977) grain-size distribution,  $N(a) \propto a^{-q}$  with  $q = 3.5$ , and a grain-size range of  $5.0 \times 10^{-3} \leq a_{\text{grain}}(\mu\text{m}) \leq 2.5 \times 10^{-1}$ . The input radiation field was represented by a single 2300 K Planckian (blackbody) source commensurate with a L3 supergiant, having an effective temperature of 2300 K (Loebman et al. 2015). A spherical shell of dust was illuminated by this source, where the dust temperature at the shell inner boundary was set at 400 K having a dust density distribution described by a inverse power law ( $\alpha = 2$ , assuming a constant wind scenario) with the shell extending 2.5 times the inner radius ( $Y = 2.5$ ). Added to this was a disk illuminated the same source with the temperature at the outer disk+envelope boundary set to 25 K, with no accretion. The grids also comprised a range of optical depths, specified at  $0.55 \mu\text{m}$ , varying in step size from 0.01–0.1 spanning  $0.5 \leq \tau_{0.55} \leq 5.0$ . A bolometric flux (scaling factor) of  $3.1 \times 10^{-11} \text{ W cm}^{-2}$  was adopted (see Appendix discussion in Jurkic & Kotnik-Karuza 2012).

### 3.4. Model Outcomes and Interpretation

Initial analysis of the mid-infrared observational data of V838 Mon suggest that the SED of the system at present can be explained as the sum of at least two components. The first is a cool central star at  $\sim 2300$  K which is likely the central remnant of the merger. The SED of this component behaves as a blackbody at 2300 K with a dusty envelope of modest optical depth such that the emergent radiation, modeled under assumptions of spherical geometry plus a disk, reasonably (in the  $\chi^2$  sense) reproduces the SEDs. The second component is emission from dust in the disk+envelope.

The emergence of a 10 μm dust feature was first observed in the 2008 Spitzer observations. Clearly, this silicate emission feature at  $\sim 10$  μm has arisen newly formed in the intervening 3 yr since 2005 (Figure 4). This 10 μm feature could arise from a combination of silicate dust (peaking at 9.7 μm) and alumina dust (peaking at 11.3 μm). More sophisticated RT modeling is required to robustly conclude whether the feature is composed purely of silicates or alumina or a combination of both, and to determine the constraints on the grain-size distribution power law.

Figure 5(a) shows the DUSTY-DISK models with range of silicate-to-alumina ratio mixes (Si:Alumina) with  $\tau_{0.55} = 1.50$ , which illustrate how variation in the dust grain components alter the the shape and structure of the model SED. The best fit to the shape of the 10 μm region at this epoch is one with Si: Alumina = 0.2:0.8, suggesting that alumina dust dominates at this epoch (2008). In order to account for additional emission longward of 20 μm a third component contributing to the overall model emission was necessary. This component is characterized by thermal continuum emission likely from dust with a  $T_{\text{bb}} \approx 170$  K, as shown in Figure 5(b). This cooler component may be associated with the cool circumstellar

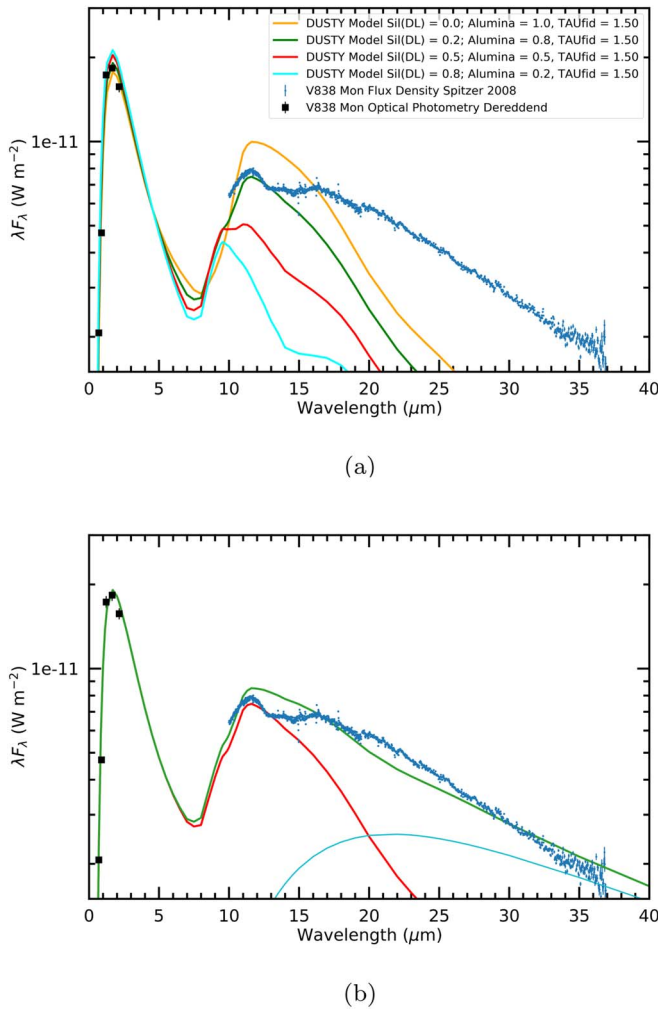


**Figure 5.** DUSTY-DISK models of V838 Mon 2008 Spitzer spectrum. The Spitzer spectrum is depicted by the blue dots, while the dereddened optical and infrared photometry are the black squares. (a) Representative sample of grid models illustrating the effect on varying the silicate-to-alumina dust ratios at a fixed optical depth  $\tau_{0.55} = 1.50$ . (b) Best-fit model composite spectra (solid green line) that includes a grain mixture ratio Si:Alumina = 0.2:0.8, emission from 2300 K blackbody representing the stellar emission (red solid curve), and a third contribution to the composite SED from a  $\approx 170$  K blackbody (cyan line). The latter is necessary to account for the observed continuum emission at wavelengths  $\gtrsim 20 \mu\text{m}$ . The dereddened optical photometry is given by the black squares.

material detected by ALMA (Kamiński et al. 2021). The sum of these three components gives a reasonable overall fit to the SED. However, the plateau between 13 and 15  $\mu\text{m}$  in the observed Spitzer spectra could not be adequately reproduced by any combination of grain composition or size distributions.

The evolution of the 10  $\mu\text{m}$  region of the SED of V838 Mon has continued and demonstrates that the chemistry of the circumstellar environment has changed over approximately the last decade. The 2019 SOFIA spectrum shows that the emission plateau from 13–15  $\mu\text{m}$  has developed into a deep trough, the width of the broad 10  $\mu\text{m}$  feature has narrowed ( $\Delta\lambda \lesssim 2.0 \mu\text{m}$ ) becoming more distinct, while an apparent absorption feature shortward of 10  $\mu\text{m}$  is seen (Figure 4(c)). This absorption may be a signature of silicates or more likely an artifact caused by imperfect removal of the deep telluric feature that lies between 8 and 10  $\mu\text{m}$  (Figure 1(b)). In other oxygen-rich environments, a deep 9.7  $\mu\text{m}$  absorption feature is attributed to SiO materials

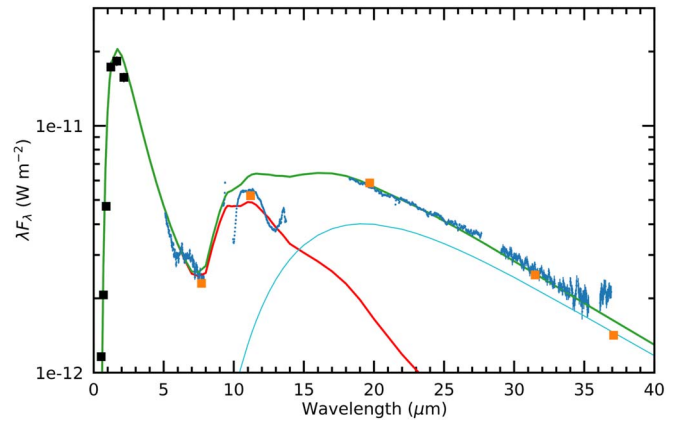


**Figure 6.** DUSTY-DISK models of V838 Mon SOFIA2019 spectrum. The SOFIA spectra are depicted by the blue dots, while the dereddened optical and infrared photometry are the black squares. The SOFIA photometry (Table 2) is indicated by the orange squares. Reasonable fit to the observed spectrum is achieved with a silicate-to-alumina ratio of order 50:50, optical depth  $\tau_{0.55} = 1.44$ . The model composite spectra (solid green line) includes model emission from the grain mixture, a 2300 K blackbody representing the stellar emission (red solid curve), and requires a third contribution to the composite SED from a  $\approx 125$  K emissivity modified ( $\epsilon_\lambda \propto \lambda^{-2}$ ) blackbody (cyan line). The latter contribution is necessary to account for the observed continuum emission at wavelengths  $\gtrsim 20 \mu\text{m}$ .

and the depth of the feature indicates that silicates may now be the dominant grain component.

In other merger-system nova likes that have dusty circumstellar envelopes, such as V1309 Sco, the broad spectral feature at 9.7  $\mu\text{m}$  is attributed to silicate grain solid-state absorption (Nicholls et al. 2013). Our models of V838 Mon require amorphous silicates and the observed SED suggests a dust absorption feature indicative of an optically thick circumstellar environment is present. Following the arguments discussed in Nicholls et al. (2013) an upper limit to the column density in V838 Mon can be derived from the observed depth of the 9.7  $\mu\text{m}$  feature (upper limit of  $\sim 2.4 \times 10^{-12} \text{ W m}^{-2}$ ) and the best-fit model continuum ( $\sim 4.6 \times 10^{-12} \text{ W m}^{-2}$ ) at the same wavelength, which yields an optical depth  $\tau_{9.7} \sim 0.3$ . Using values of  $Q_{\text{ext}}$  and  $Q_{\text{scat}}$  for “astronomical silicate” taken from Draine (1985) and assuming amorphous silicate grains with radii  $a$  between 0.1 and 3.0  $\mu\text{m}$  (the upper limit to  $a$  is set by the transition to a regime where the 9.7  $\mu\text{m}$  feature is suppressed; see Figure 5 in Laor & Draine 1993) leads to a derived column density of between  $\sim 8 \times 10^8 \text{ cm}^{-2}$  to  $2 \times 10^{10} \text{ cm}^{-2}$ .

The rise of silicates also is supported by the shape and strength of the broad 10  $\mu\text{m}$  band emission. This speculation is confirmed by DUSTY-DISK modeling of the 2019 SOFIA composite spectra, as shown in Figure 6. Models that best reproduce the 10  $\mu\text{m}$  feature are those where the Si:Alumina ratio is now at least 50:50, with a slight decrease in the optical depth to  $\tau_{0.55} = 1.44$ . A cooler third component with  $T_{\text{bb}} = 125 \text{ K}$  and a wavelength dependent emissivity  $\epsilon \propto \lambda^{-2}$  at wavelengths  $\gtrsim 10 \mu\text{m}$  are thought to be present. The observed spectral evolution indicates that processing of the dust in V838 Mon is occurring, perhaps similar to that in the environs of V1309 Sco (Nicholls et al. 2013).

Clearly, there is a temporal evolution of this 10  $\mu\text{m}$  feature with the relative strengths of the silicate and alumina components evolving with time in a manner consistent with the chaotic silicate hypothesis of mineral condensation described by Nuth & Hecht (1990) or other models based on



thermodynamically controlled evolution (Speck et al. 2000). The model fits (Figures 5 and 6) while not totally satisfactory, do permit two possible interpretations. First, there was a significant amount of alumina in the  $10\ \mu\text{m}$  feature when this feature first developed. Modeling suggests that the Si:Alumina ratio was  $\gtrsim 0.5$ . This would be observational evidence which supports the prediction that alumina should be the first dust condensate in an O-rich environment. Evidence for this prediction is rarely offered because most objects studied (e.g., Miras, AGB stars, etc.) are millions of years old. In the present case one is seeing this event happen in freshly condensed dust and almost in real time. The temporal sequence of dust evolution in V383Mon may be a rare validation of mineralogical condensation sequences (Nuth & Hecht 1990) occurring in O-rich environments, perhaps only seen before in V4332 Sgr (Banerjee et al. 2007).

Alternatively, one could conclude that the Si:Alumina ratio changed between 2008 and 2019. It appears that the silicate fraction within the dust population has increased by  $\gtrsim 30\%$ . The increase of silicate with time, at the expense of alumina, can be explained as follows (e.g., Nuth & Hecht 1990; Stencel et al. 1990): in the initial stages, the higher reduction of Al with respect to Si leads to the preferential formation of Al–O bonds at the expense of Si–O bonds. This implies that the infrared bands of alumina associated with the Al–O stretching mode should be prominent early in the formation of the chaotic silicates. However, as the Al atoms become fully oxidized, the higher abundance of Si will make the  $9.7\ \mu\text{m}$  band associated with Si–O bonds dominate.

The presence of alumina as a dust component is not surprising. V838 Mon is known to exhibit strong photospheric B–X infrared bands of AlO in the infrared (Banerjee & Ashok 2002; Evans et al. 2003; Lynch et al. 2004), which are present even today (as seen in the recent SOFIA spectra discussed herein). Aluminum oxide is likely to play a significant role in the route to  $\text{Al}_2\text{O}_3$  formation. LTE calculations by Gail & Sedlmayr (1999) show that any possible nucleation species that can go on to form dust around stars should begin with a monomer with exceptionally high bond energy. The AlO monomer satisfies this criterion and is thus a favored candidate to lead to the formation of larger  $\text{Al}_m\text{O}_n$  clusters that serve as nucleation sites for the formation of other grains or to alumina grains themselves by homogeneous nucleation.

We have not considered in our model the effect of ongoing processes such as annealing of the dust or grain growth. Annealing of silicate grains can change the optical constants of the grain significantly, as shown by the study of Hallenbeck et al. (2000) and this can result in changes in the shape and peak of the silicate profile. This point becomes relevant when comparing the evolution of dust features across different epochs. The physics of grain growth in the expanding ejecta of novae, where the radiation field may be similar to the early conditions in V838 Mon, is explored by Shore & Gehrz (2004).

#### 4. Summary

Over the last decade the dust chemistry in the circumstellar environment of V838 Mon has dynamically evolved. The temporal changes observed in the  $10\ \mu\text{m}$  is evidence of a “classical” dust condensation sequence expected to occur in dense oxygen-rich regions. Further synoptic study of V838 Mon in the infrared with SOFIA and JWST are required






to explore timescales for condensation pathways, to ascertain the nature of the colder component contributing to the spectral energy distribution at wavelengths  $\gtrsim 20\ \mu\text{m}$ , and to understand the spatial distribution of the circumstellar emission.

The authors would like to thank Zeljko Ivezić for the helpful insight into the DUSTY and DUST-DISK codes, and Floretin Millour for discussion of V838 Mon spectra in the  $10\ \mu\text{m}$  region. The authors also appreciate the thoughtful critique and suggestions by the referee, which improved the manuscript. This work is based in part on observations made with the NASA/DLR Stratospheric Observatory for Infrared Astronomy (SOFIA). SOFIA is jointly operated by the Universities Space Research Association, Inc. (USRA), under NASA contract NNA17BF53C, and the Deutsches SOFIA Institut (DSI) under DLR contract 50 OK 0901 to the University of Stuttgart. Also based on observations made with the Nordic Optical Telescope, owned in collaboration by the University of Turku and Aarhus University, and operated jointly by Aarhus University, the University of Turku, and the University of Oslo—representing Denmark, Finland, and Norway—the University of Iceland and Stockholm University at the Observatorio del Roque de los Muchachos, La Palma, Spain, of the Instituto de Astrofísica de Canarias. Financial support for this work and C.E.W. was provided by NASA through award SOF07-0027 issued by USRA to the University of Minnesota. D.P.K.B. is supported by a CSIR Emeritus Scientist grant in aid, which is hosted by the Physical Research Laboratory, Ahmedabad. The Astronomical Institute of the Czech Academy of Sciences is supported by the project RVO:67985815. We acknowledge with thanks the variable star observations from the AAVSO International Database contributed by observers worldwide and used in this research. R.D.G. was supported by the United States Air Force.

*Facilities:* NASA SOFIA (FORCAST), NASA Spitzer (IRS), AAVSO, IRSA, IPAC, NOT.

*Software:* IRAF, REDUX (Clarke et al. 2015), APT (Laher et al. 2012), astropy (Astropy Collaboration et al. 2018).

#### ORCID iDs

C. E. Woodward  <https://orcid.org/0000-0001-6567-627X>  
 A. Evans  <https://orcid.org/0000-0002-3142-8953>  
 D. P. K. Banerjee  <https://orcid.org/0000-0003-4896-2543>  
 T. Liimets  <https://orcid.org/0000-0003-2196-9091>  
 A. A. Djupvik  <https://orcid.org/0000-0001-6316-9880>  
 S. Starrfield  <https://orcid.org/0000-0002-1359-6312>  
 G. C. Clayton  <https://orcid.org/0000-0002-0141-7436>  
 S. P. S. Eyres  <https://orcid.org/0000-0002-6663-7675>  
 R. D. Gehrz  <https://orcid.org/0000-0003-1319-4089>  
 R. M. Wagner  <https://orcid.org/0000-0003-1892-2751>

#### References

- Abbott, T. M., Aspin, C., Sorensen, A. N., et al. 2000, *Proc. SPIE*, **4008**, 714
- Astropy Collaboration, Price-Whelan, A. M., Sipőcz, B. M., et al. 2018, *AJ*, **156**, 123
- Banerjee, D. P. K., & Ashok, N. M. 2002, *A&A*, **395**, 161
- Banerjee, D. P. K., Barber, R. J., Ashok, N. M., & Tennyson, J. 2005, *ApJL*, **627**, L141
- Banerjee, D. P. K., Misselt, K. A., Su, K. Y. L., Ashok, N. M., & Smith, P. S. 2007, *ApJL*, **666**, L25
- Banerjee, D. P. K., Su, K. Y. L., Misselt, K. A., & Ashok, N. M. 2006, *ApJL*, **644**, L57
- Banerjee, D. P. K., Nuth, J. A. I., Misselt, K. A., et al. 2015, *ApJ*, **814**, 109



- Begemann, B., Dorschner, J., Henning, T., et al. 1997, *ApJ*, **476**, 199
- Bond, H. E., & Siegel, M. H. 2006, *AJ*, **131**, 984
- Bond, H. E., Henden, A., Levay, Z. G., et al. 2003, *Natur*, **422**, 405
- Brown, N. J., Waagen, E. O., Scovill, C., et al. 2002, *IAU Circ.*, **7785**, 1
- Chesneau, O., Millour, F., De Marco, O., et al. 2014, *A&A*, **569**, L3
- Clarke, M., Vacca, W. D., & Shuping, R. Y. 2015, in *ASP Conf. Ser.*, 495, Redux: A Common Interface for SOFIA Data Reduction Pipelines, ed. Taylor & Rosolowsky (San Francisco, CA: ASP), 355
- Draine, B. T. 1985, *ApJS*, **57**, 587
- Draine, B. T., & Lee, H. M. 1984, *ApJ*, **285**, 89
- Evans, A., Geballe, T. R., Rushton, M. T., et al. 2003, *MNRAS*, **343**, 1054
- Evans, A., & Gehr, R. D. 2012, *BASI*, **40**, 213
- Exter, K. M., Cox, N. L. J., Swinyard, B. M., et al. 2016, *A&A*, **596**, A96
- Gail, H.-P., & Hoppe, P. 2010, in *The Origins of Protoplanetary Dust and the Formation of Accretion Disks*, ed. D. A. Apai & D. S. Lauretta (Cambridge: Cambridge Univ. Press), 27
- Gail, H. P., & Sedlmayr, E. 1999, *A&A*, **347**, 594
- Gehr, R. D., Becklin, E. E., de Pater, I., et al. 2009, *AdSpR*, **44**, 413
- Gehr, R. D., Evans, A., Helton, L. A., et al. 2015, *ApJ*, **812**, 132
- Hallenbeck, S. L., Nuth, J. A. I., & Nelson, R. N. 2000, *ApJ*, **535**, 247
- Helton, L. A., Gehr, R. D., Woodward, C. E., et al. 2012, *ApJ*, **755**, 37
- Herter, T. L., Adams, J. D., Gull, G. E., et al. 2018, *JAI*, **7**, 1840005
- Hillen, M., Menu, J., Van Winckel, H., et al. 2014, *A&A*, **568**, A12
- Houck, J. R., Roellig, T. L., Van Cleve, J., et al. 2004, *Proc. SPIE*, **5487**, 62
- Ivezic, Z., & Elitzur, M. 1995, *ApJ*, **445**, 415
- Jurkic, T., & Kotnik-Karuza, D. 2012, *A&A*, **544**, A35
- Kafka, S. 2020, in *European Planetary Science Congress EPSC2020-314*
- Kamiński, T., Steffen, W., Tylenda, R., et al. 2018, *A&A*, **617**, A129
- Kamiński, T., Tylenda, R., Kiljan, A., et al. 2021, *arXiv:2106.07427*
- Karovicova, I., Wittkowski, M., Ohnaka, K., et al. 2013, *A&A*, **560**, A75
- Kasliwal, M. M. 2012, *PASA*, **29**, 482
- Laher, R. R., Gorjian, V., Rebull, L. M., et al. 2012, *PASP*, **124**, 737
- Laor, A., & Draine, B. T. 1993, *ApJ*, **402**, 441
- Lebouteiller, V., Barry, D. J., Goes, C., et al. 2015, *ApJS*, **218**, 21
- Lebouteiller, V., Barry, D. J., Spoon, H. W. W., et al. 2011, *ApJS*, **196**, 8
- Loebman, S. R., Wisniewski, J. P., Schmidt, S. J., et al. 2015, *AJ*, **149**, 17
- Lynch, D. K., Rudy, R. J., Russell, R. W., et al. 2004, *ApJ*, **607**, 460
- MacLeod, M., & Loeb, A. 2020, *ApJ*, **893**, 106
- Mathis, J. S., Rumpl, W., & Nordsieck, K. H. 1977, *ApJ*, **217**, 425
- Nicholls, C. P., Melis, C., Soszynski, I., et al. 2013, *MNRAS*, **431**, L33
- Nuth, J. A. I., & Hecht, J. H. 1990, *Ap&SS*, **163**, 79
- Ortiz-León, G. N., Menten, K. M., Kamiński, T., et al. 2020, *A&A*, **638**, A17
- Pastorello, A., Mason, E., Taubenberger, S., et al. 2019, *A&A*, **630**, A75
- Pastorello, A., Fraser, M., Valerin, G., et al. 2021, *A&A*, **646**, A119
- Posch, T., Kerschbaum, F., Mutschke, H., Dorschner, J., & Jäger, C. 2002, *A&A*, **393**, L7
- Posch, T., Kerschbaum, F., Mutschke, H., et al. 1999, *A&A*, **352**, 609
- Richter, M. J., Dewitt, C. N., McKelvey, M., et al. 2018, *JAI*, **7**, 1840013
- Rieke, G. H., & Lebofsky, M. J. 1985, *ApJ*, **288**, 618
- Sargent, B. A., Forrest, W., Watson, D. M., et al. 2014, *ApJ*, **792**, 83
- Shore, S. N., & Gehr, R. D. 2004, *A&A*, **417**, 695
- Smith, N., Andrews, J. E., Van Dyk, S. D., et al. 2016, *MNRAS*, **458**, 950
- Sparks, W. B., Bond, H. E., Cracraft, M., et al. 2008, *AJ*, **135**, 605
- Speck, A. K., Barlow, M. J., Sylvester, R. J., & Hofmeister, A. M. 2000, *A&AS*, **146**, 437
- Stencel, R. E., Nuth, J. A. I., Little-Marenin, I. R., & Little, S. J. 1990, *ApJL*, **350**, L45
- Tielens, A. G. G. M. 1990, in *From Miras to Planetary Nebulae: Which Path for Stellar Evolution?* ed. M. O. Mennessier & A. Omont (Gif sur Yvette: Editions Frontieres), 186
- Tielens, A. G. G. M., Waters, L. B. F. M., Molster, F. J., & Justtanont, K. 1998, *Ap&SS*, **255**, 415
- Tylenda, R., & Soker, N. 2006, *A&A*, **451**, 223
- Williams, S. C., Darnley, M. J., Bode, M. F., & Steele, I. A. 2015, *ApJL*, **805**, L18
- Young, E. T., Becklin, E. E., Marcum, P. M., et al. 2012, *ApJL*, **749**, L17
- Zeidler, S., Posch, T., & Mutschke, H. 2013, *A&A*, **553**, A81